Harmonic signals of magnetic nanoparticle in suspension for biosensing application: Comparison of properties between Brownian- and Néel-dominant regions

Enpuku, Keiji
Department of Electrical and Electronic Engineering, Kyushu University

Sun, Yi
Department of Electrical and Electronic Engineering, Kyushu University

Zhang, Haochen
Department of Electrical and Electronic Engineering, Kyushu University

Yoshida, Takashi
Department of Electrical and Electronic Engineering, Kyushu University

出版情報：Journal of Magnetism and Magnetic Materials. 579, pp.170878-, 2023-08-01. Elsevier
バージョン：
権利関係：

Harmonic signals of magnetic nanoparticle in suspension for biosensing application: Comparison of properties between Brownian- and Néel-dominant regions

Keiji Enpuku*, Yi Sun, Haochen Zhang, and Takashi Yoshida

Department of Electrical and Electronic Engineering, Kyushu University, Fukuoka 819-0395, Japan

Abstract

We have studied harmonic signals caused by the nonlinear AC magnetization (*M–H*) curve of magnetic nanoparticles (MNPs) suspended in solution. First, numerical simulations were performed for wide ranges of the MNP parameters and the excitation fields that are commonly used in biosensing applications. As an example, the third harmonic signal was mainly studied. Because the AC *M–H* curve for the suspended MNPs is affected by both Brownian and Néel relaxations, we demonstrated the condition that determines the dominant relaxation. We emphasize that the MNP's behavior changes from Brownian-dominant to Néel-dominant relaxation when the amplitude of the excitation field is increased, even when the MNP parameters are fixed. The properties of the harmonic signals in the Brownian- and Néel-dominant cases were compared, and the differences between the two cases were clarified. The relationships among the higher harmonic signals were also presented. Next, an analytical expression for the third harmonic signal was obtained for both the Brownian- and Néel-dominant cases. In the Néel-dominant case, the alignment of the easy axes caused by the AC field was taken into account. We demonstrated good agreement between the simulation and the analysis results. Finally, harmonic signals were measured using a commercial MNPs sample. Reasonable agreement was obtained between experiment and analysis. The results obtained will be useful for biosensing applications.

Keywords

Magnetic nanoparticle; Néel relaxation; Brownian relaxation; harmonic signal; easy axis alignment; magnetic biosensing

1. Introduction

Harmonic signals caused by the nonlinear AC magnetization (*M–H*) curve of magnetic nanoparticles (MNPs) have been studied widely for biosensing applications. These signals have been used to develop a magnetic particle imaging (MPI) system, where the three-dimensional positions of the MNPs can be detected with high temporal resolution for medical diagnosis [1-5]. The signals are also used in magnetic biosensing, where disease-related biological targets can be detected using bio-functionalized MNPs [6-13].

In biosensing applications, the MNPs are used in three states, i.e., suspended in solution, immobilized, and fixed on biological targets. When the MNPs are immobilized, physical rotation of the MNPs caused by Brownian relaxation is prohibited. In this case, the AC *M–H* curve is determined by Néel relaxation alone. When the MNPs are fixed on targets whose size is very much larger than the MNPs, e.g. for the case of cells, the MNPs can also be approximated by the immobilized ones. This is because physical rotation of the fixed MNPs is determined by the Brownian relaxation time of the cell, which can be estimated as long as 10 s for the 3 μm-size cell. In this case, the AC *M–H* curve is also determined by Néel relaxation alone. For suspended MNPs, however, both Brownian and Néel relaxations affect the AC *M–H* curve. This also occurs when the MNPs are fixed on targets whose size is comparable or smaller than the MNPs, such as disease-related proteins. In these cases, the MNP parameters and the excitation conditions determine which relaxation type occurs faster and thus becomes dominant. As a result, the magnetic properties of the suspended MNPs are considerably more complex when compared to the immobilized MNPs case.

The dominant relaxation for the suspended MNPs is determined by the magnitude relationship between their two relaxation times [14, 15]. There are two limiting cases for this relationship. The first is $\tau_N(H) >> \tau_B(H)$, where $\tau_N(H)$ and $\tau_B(H)$ are the field-dependent Néel and Brownian relaxation times, respectively. In this case, the AC *M–H* curve is determined by the Brownian relaxation [16]. The second case is $\tau_N(H) << \tau_B(H)$. In this case, dynamics of the magnetic moment vector $\boldsymbol{m}$ of the suspended MNPs is primarily dominated by Néel relaxation. In addition, successive physical rotation of MNPs occurs partially for high field amplitude, which causes rotation of the easy axis of magnetization in suspended MNPs. Due to this two-step relaxation process, partial alignment of the easy axes is caused by the AC field [17-19]. The effect of easy axes alignment on the AC *M–H* curve has been studied both experimentally and theoretically [20-27].

In our previous paper, we showed that the MNP's behavior changes from Brownian-dominant to Néel-dominant when the amplitude of the excitation field H is increased, even when the MNP parameters are fixed [15]. This occurs because the reduction in τ_N with increasing H is much more significant than the reduction of τ_B. Because the change in the dominant relaxation mechanism causes the difference in the harmonic signals, it is necessary to quantitatively clarify the differences between the properties of the Brownian- and Néel-dominant cases. This characterization is very important when

MNPs are used in biosensing applications.

In this paper, we study the extent to which Brownian or Néel relaxation contributes to the harmonic signals of the suspended MNPs. First, we discuss the condition under which either the Brownian or Néel relaxation becomes dominant. Then, numerical simulations are performed for wide ranges of the MNP parameters and excitation fields that are commonly used in biosensing. As an example, the third harmonic signal was mainly studied. The dependences of the third harmonic signal on the MNP parameters and the excitation field were obtained, and the differences between the Brownian- and Néel-dominant cases were clarified. The relationships among the higher harmonic signals were also demonstrated. Next, analytical expressions for the third harmonic signal were obtained for both the Brownian- and Néel-dominant cases. In the Néel-dominant case, the alignment of the easy axes caused by the AC field was taken into account. Finally, the properties of the harmonic signals were measured using a commercial MNPs sample. Reasonable agreement was obtained between experiments and analyses.

2. Materials and methods

Numerical simulations of the AC $M-H$ curves are performed for both the immobilized and suspended MNPs when the sinusoidal excitation field $H(t) = H_{ac}\sin(2\pi ft)$ is applied, where H_{ac} and f are the amplitude and frequency of the excitation field, respectively. In the simulation, we assumed that concentration of the MNPs is low, and neglected the magnetic dipole-dipole interactions among the MNPs. For the immobilized MNPs, where the easy axes are fixed regardless of time and are randomly oriented, we solved for the dynamics of the magnetic moment vector $\boldsymbol{m}$ using the Fokker-Planck equation. For the suspended MNPs, we solved for both the dynamics of $\boldsymbol{m}$ and the unit vector along the easy axis $\boldsymbol{n}$ simultaneously using the stochastic Landau–Lifshitz–Gilbert equation and an equation from *Usov et al.* [28]. Net magnetization of an ensemble of MNPs in the direction of the excitation field was calculated to obtained $M(t)$. Details of the simulation procedure are given in our previous papers [21, 23].

Numerical simulations were performed for wide ranges of the MNP parameters and the excitation fields that are normally used for biosensing. We considered the case when the MNPs are operated at room temperature, and fixed the absolute temperature as $T = 300$ K. When we assume a homogeneous magnetic core, MNP parameters are the saturation magnetization M_s, the effective magnetic anisotropy constant K, and diameter of the magnetic core d_c. It is well known that the dynamic behavior of the MNPs is determined by the values of $\sigma = KV_c/(k_BT)$ and $\xi_{ac} = \mu_0 H_{ac} m/(k_BT)$, where $V_c = (\pi/6)d_c^3$ and $m = M_s V_c$ are the volume of the magnetic core and magnetic moment of the MNP, respectively, and k_B is the Boltzmann constant. Note that σ represents the energy ratio between anisotropy energy and thermal energy, while ξ_{ac} represents the ratio between magnetic energy and thermal energy. We note that ξ_{ac} can be expressed as $\xi_{ac} = 2\sigma h_{ac}$, where $h_{ac} = H_{ac}/H_k$ is the field normalized by $H_k = 2K/(\mu_0 M_s)$.

In the simulation, the σ value was varied from 7 to 20. For each σ, the h_{ac} value was varied from 0.1 to 0.5. Because $\xi_{ac}=2\sigma h_{ac}$, the ξ_{ac} value was varied from 0.2σ to 1.0σ for each σ value. We note that the ratio between anisotropy energy and magnetic energy, which is given by $\lambda=(KV)/(\mu_0 H_{ac} m)=1/(2h_{ac})$, was varies from 5 to 1. If we assume that M_s = 350 kA/m and K = 10 kJ/m^3, the simulation is then performed for 17.7 nm < d_c < 25.1 nm and 5.7 mT < $\mu_0 H_{ac}$ < 28.6 mT. The frequency was varied from f = 1 kHz to 50 kHz. The hydrodynamic diameter of an MNP is fixed as d_H = 50 nm. The Brownian relaxation time is given by $\tau_{B,0} = 3\eta V_H/(k_B T)$, where η is the liquid viscosity, and $V_H = (\pi/6)d_H^3$ is the hydrodynamic volume of the MNP; we note that $\tau_{B,0}$ can be interpreted by using an energy ratio as $\tau_{B,0} = (T_m/k_B T)/\omega$, where $T_m=3\eta V_H\omega$ is the mechanical torque, and ω is the angular velocity of the MNP. We obtain $\tau_{B,0}$ = 48 μs for η = 1 mPa·s, d_H = 50 nm and T = 300 K.

From the numerical simulations, the waveform of $M(t)$ is obtained. Then, the harmonic signals were obtained by expanding $M(t)$ into a Fourier series. In this study, the third harmonic signal was mainly studied. This approach was used because the fundamental component is usually excluded from biosensing applications to avoid interference from the excitation field. Note that the imaginary part of the fundamental component, which gives the hysteresis area in the *M-H* curve, was studied in our previous paper for hyperthermia applications [15, 27].

In the experiment, we used a commercial MNPs sample called Synomag (micromod GmbH, Germany). Synomag consists of maghemite (γ-Fe_2O_3) cores covered with a dextran shell with nominal value of d_H = 50 nm. We choose the Synomag sample because it has been used for MPI. This sample is also suitable for comparison between experiment and analysis because the distributions of d_c and d_H are relatively small. The magnetic parameters were estimated to be M_s = 345 kA/m and K = 9.7 kJ/m^3 [15]. In the experiments, 150 μg-Fe of MNPs were dispersed in 150 μL of water for the suspended sample. For the immobilized samples, 150 μg-Fe of MNPs were dispersed in 150 μL of epoxy resin and then solidified with randomly oriented easy axes [22]. The AC *M–H* curves were measured using a homemade measurement system, which we described in detail in our previous paper [29].

3. Numerical simulations

3.1 *Conditions for the Néel- and Brownian-dominant regions*

First, we show the condition under which either the Brownian or Néel relaxation becomes dominant. As discussed in our previous paper [15], the condition can be obtained by comparing the field dependent relaxation times $\tau_B(H)$ and $\tau_N(H)$. The expression for $\tau_B(H)$ is given by [16, 30]:

$$\tau_B(H) = \frac{\tau_{B,0}}{\sqrt{1+0.07\xi_{ac}^2}}. \quad (1)$$

The expression for $\tau_N(H)$ is given by [31]:

$$\tau_N(H) = \frac{\tau_0\sqrt{\pi}}{\sqrt{\sigma}(1-h^2)} \frac{1}{(1+h)e^{-\sigma(1+h)^2} + (1-h)e^{-\sigma(1-h)^2}}, \quad (2)$$

where $h = H/H_k$ is the normalized field. In this study, we use Eq. (2) for simplicity, although Eq. (2) is obtained when the easy axis lies parallel to the applied field. We also set $h = h_{ac} = H_{ac}/H_k$ in Eq. (2) to study the Néel relaxation time when AC field was applied.

As can be seen from Eqs. (1) and (2), $\tau_B(H)$ and $\tau_N(H)$ are determined by σ and h_{ac} because $\xi_{ac}=2\sigma h_{ac}$. Therefore, we can discuss the condition under which either the Brownian or Néel relaxation becomes dominant using the σ–h_{ac} plane [15].

Fig. 1 shows the four regions in the σ–h_{ac} plane that determine the dominant relaxation. Fig. 1(a) was calculated for $f = 20$ kHz and $d_H = 50$ nm, while Fig. 1(b) was calculated for $f = 3$ kHz and $d_H = 50$ nm. As shown in Fig. 1(a), the σ–h_{ac} plane can be divided into four regions for $f = 20$ kHz and $d_H = 50$ nm.

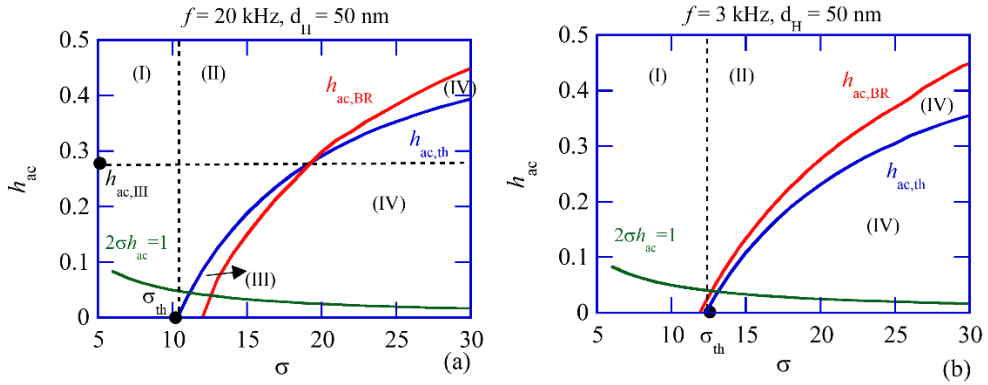

Fig. 1. Four regions in the σ–h_{ac} plane that determine the dominant relaxation. (a) $f = 20$ kHz and $d_H = 50$ nm, and (b) $f = 3$ kHz and $d_H = 50$ nm. In regions (I) and (II), Néel relaxation becomes dominant. In region (III), both Brownian and Néel relaxations contribute. In region (IV), Brownian relaxation becomes dominant. Blue and red lines represent $h_{ac} = h_{ac,th}$ and $h_{ac} = h_{ac,BR}$ given in Eqs. (4) and (5), respectively. Green line is given by $2\sigma h_{ac} = 1$. The boundary for each region is given by σ_{th}, $h_{ac,th}$, $h_{ac,BR}$, and $h_{ac,III}$.

Region (I) in Fig. 1(a) is determined by the condition that $\sigma < \sigma_{th}$; here, $\sigma_{th} = 10.3$ for $f = 20$ kHz. The value of σ_{th} is given by the condition that $2\pi f\tau_{N,0}(\sigma_{th}) = 1$, where $\tau_{N,0}$ is the Néel relaxation time given by $\tau_{N,0}(\sigma) = \sqrt{\pi/\sigma}\tau_0 \exp(\sigma)/2$, and $\tau_0 = 10^{-9}$ s is the characteristic time [27]. The value of σ_{th} is determined by the frequency f, and an explicit expression for σ_{th} can be obtained in an approximate form as:

$$\sigma_{th} = 0.86 - 1.05 \times \ln(2\pi f\tau_0). \quad (3)$$

In region (I), the condition $2\pi f\tau_{N,0} < 1$ is satisfied, and Néel relaxation thus dominates the MNPs dynamics for all h_{ac} values.

When $\sigma > \sigma_{\text{th}}$, three regions, i.e., regions (II)-(IV), exist depending on the value of h_{ac}. The boundaries between the regions are given by $h_{\text{ac,th}}$ and $h_{\text{ac,BR}}$, as shown below.

The field $h_{\text{ac,th}}$ is given by the condition $\tau_N(h_{\text{ac,th}}) = 1/(2\pi f)$, and is determined by σ and f. An explicit expression was obtained as follows [27]:

$$h_{\text{ac,th}} = \begin{cases} 0 & \text{for } \sigma \le \sigma_{\text{th}}, \\ 0.6\left(1 - \dfrac{\sigma_{\text{th}}}{\sigma}\right) & \text{for } \sigma > \sigma_{\text{th}} \end{cases} \quad (4)$$

The field $h_{\text{ac,BR}}$ is given by the condition $\tau_N(h_{\text{ac,BR}}) = \tau_B(h_{\text{ac,BR}})$, and an approximate expression for this field can be given as:

$$h_{\text{ac,BR}} = 1 - \left[\frac{\ln(2 \times 10^9 \tau_{B.0})}{\sigma}\right]^{0.62} \quad (5)$$

Note that $h_{\text{ac,BR}}$ depends on both σ and $\tau_{B,0}$, but is independent of f.

As shown in Fig. 1(a), the $h_{\text{ac,th}}$–σ and $h_{\text{ac,BR}}$–σ curves intersect at $h_{\text{ac}} = h_{\text{ac,III}}$. Note that the following condition is satisfied at $h_{\text{ac}} = h_{\text{ac,III}}$:

$$\frac{1}{2\pi f} = \tau_N\left(h_{\text{ac,III}}\right) = \tau_B\left(h_{\text{ac,III}}\right) \quad (6)$$

Region (II) in Fig. 1(a) is determined by the field that satisfies both $h_{\text{ac}} > h_{\text{ac,th}}$ and $h_{\text{ac}} > h_{\text{ac,BR}}$. For this field, the conditions $\tau_N(H) < 1/(2\pi f)$ and $\tau_N(H) < \tau_B(H)$ are satisfied. In region (II), therefore, Néel relaxation is dominant, and the magnetic moment of the MNP changes its polarity by passing the anisotropy energy barrier when the AC field is applied. Note that $h_{\text{ac,th}}$ in Eq. (4) gives the threshold field for this magnetic moment reversal over the anisotropy energy barrier. We also noted that the AC field causes successive Brownian (physical) rotation in suspended MNPs, and the easy axes are partially aligned along the AC field for the case where $\tau_N(H) < 1/(2\pi ft) < \tau_B(H)$ [23, 27]. When partial alignment occurs, the angle of the easy axis with respect to the applied field, β, converges around a specific value. This is in contrast to the case of the randomly oriented easy axis, where β is distributed uniformly from $\beta = 0$ to $\pi/2$.

Region (IV) is determined by the field $h_{\text{ac}} < h_{\text{ac,BR}}$. In this case, the condition $\tau_B(H) < \tau_N(H)$ is satisfied, and Brownian relaxation thus becomes dominant. Note, however, that the effect of Brownian relaxation only becomes large for $h_{\text{ac}} > h_{\text{ac,III}}$ because the condition $\tau_B(H) < 1/(2\pi f)$ can be satisfied for this case. When $h_{\text{ac}} < h_{\text{ac,III}}$, $\tau_B(H) > 1/(2\pi f)$ and the effect of the Brownian relaxation is small.

Region (III) is determined by the condition that $h_{\text{ac,BR}} < h_{\text{ac}} < h_{\text{ac,th}}$. This region only appears for $h_{\text{ac}} < h_{\text{ac,III}}$. In this region, both the Brownian and Néel relaxations affect the AC M–H curve of the suspended sample in a complex manner.

In Fig. 1(a), the line given by $\xi_{\text{ac}} = 2\sigma h_{\text{ac}} = 1$ is also shown. Note that the nonlinearity of the M–H curve becomes large when $\xi_{\text{ac}} >> 1$. Therefore, the field h_{ac} must satisfy the condition that $2\sigma h_{\text{ac}} >> 1$

to obtain rich harmonic signals.

Fig. 1(b) shows the result for f = 3 kHz. In this case, σ_{th} = 12.2, and $h_{\mathrm{ac,BR}} > h_{\mathrm{ac,th}}$ for all values of σ. As a result, $h_{\mathrm{ac,III}}$ does not exist, and region (III) disappears in this case. In region (IV), the condition that $\tau_B(H) < 1/(2\pi f)$ is satisfied for all h_{ac} values. Therefore, the effect of the Brownian relaxation becomes large for all h_{ac} values when f = 3 kHz.

3.2 *Third harmonic signal*

Next, we study the amplitude of the third harmonic signal, M_3, for regions (I)–(IV) in Fig. 1. As examples, we selected values of σ = 7 to study M_3 in region (I) and σ = 20 in regions (II)–(IV). Fig. 2 shows the M_3–h_{ac} curves obtained for the different sets of σ and f (kHz): (σ, f) = (7, 20), (7, 3), (20, 20) and (20, 3). The rectangles represent the simulation results for the immobilized MNPs with randomly oriented easy axes. The circles represent the results obtained for the suspended MNPs, where we selected d_{H} = 50 nm; $\tau_{B,0}$ = 48 μs for η = 1 mPa·s. The lines represent the analytical results that will be obtained in Sec. 4.

Fig. 2(a) shows the M_3–h_{ac} curves obtained for σ = 7 and f = 20 kHz. As shown, the value of M_3 for the immobilized MNPs increased gradually with increasing h_{ac}. The M_3 characteristic for the suspended MNPs was almost the same as that for the immobilized MNPs when $h_{\mathrm{ac}} < 0.2$. However, in the case where $h_{\mathrm{ac}} > 0.2$, the difference in M_3 values between the two cases increased with increasing h_{ac}. When h_{ac} = 0.5, M_3 for the suspended case was 1.5 times that of the immobilized case.

Note that the condition $\tau_{N,0} < 1/(2\pi f) << \tau_{B,0}$ is satisfied for σ = 7 and f = 20 kHz. In this case, the MNPs dynamics are determined by the Néel relaxation for all h_{ac} values, and partial alignment of the easy axes is caused in the suspended MNPs. Therefore, the difference in the M_3 characteristics between the suspended and immobilized cases was caused by the alignment of the easy axes. The red line represents the analytical $M_{3,\mathrm{NR}}$–h_{ac} curve for the immobilized case [Eqs. (12)–(15)], while the blue line represents the $M_{3,\mathrm{NA}}$–h_{ac} curve for the aligned case [Eqs. (16)–(19)]. As shown in the figure, the simulation results agreed well with these two curves.

Fig. 2(b) presents the M_3–h_{ac} curve for σ = 7 and f = 3 kHz. In this case, the M_3 characteristic for the immobilized MNPs was almost the same as that at f = 20 kHz (c.f. Fig. 2(a)). However, the M_3 characteristic for the suspended MNPs became smaller than the case for f = 20 kHz. This result indicates that the degree of alignment of the easy axes becomes smaller at f = 3 kHz. Note that $2\pi f\tau_{B,0}$ = 0.89 for f = 3 kHz, while $2\pi f\tau_{B,0} >> 1$ for f = 20 kHz. Therefore, we can expect the degree of alignment of the easy axes to be dependent on the value of $2\pi f\tau_{B,0}$. We will discuss the frequency dependence of the alignment of the easy axes in Sec. 4.

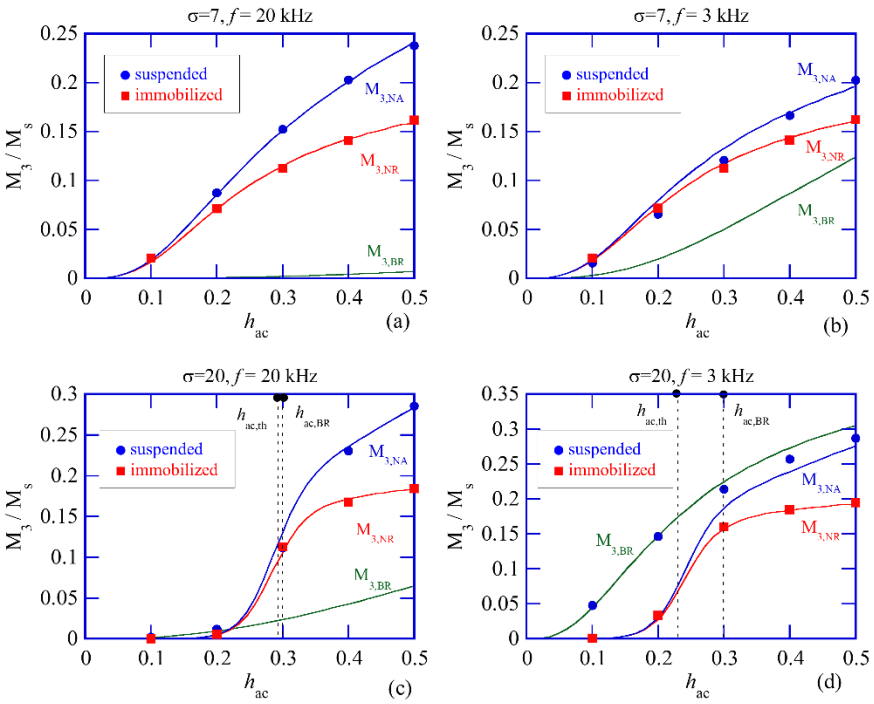

Fig. 2. M_3–h_{ac} curves. (a) $\sigma = 7$ and $f = 20$ kHz, (b) $\sigma = 7$ and $f = 3$ kHz, (c) $\sigma = 20$ and $f = 20$ kHz, and (d) $\sigma = 20$ and $f = 3$ kHz. The symbols represent the simulation results. The red line represents the analytical $M_{3,NR}$–h_{ac} curve for the immobilized case [Eqs. (12)–(15)]. The blue line represents the $M_{3,NA}$–h_{ac} curve for the aligned case [Eqs. (16)–(19)]. The green line represents the $M_{3,BR}$–h_{ac} curve for the Brownian-dominant case [Eqs. (10) and (11)].

Fig. 2(c) shows the M_3–h_{ac} curve for $\sigma = 20$ and $f = 20$ kHz. In this case, we obtained $h_{ac,th} = 0.29$ and $h_{ac,BR} = 0.30$. Therefore, for $h_{ac} < h_{ac,BR} = 0.3$, the MNPs operate in region (IV) and the Brownian relaxation becomes dominant. However, because $1/(2\pi f) << \tau_{B,0}$ for $f = 20$ kHz, the Brownian relaxation does not affect M_3 for the suspended MNPs. As a result, the difference in M_3 characteristics between the suspended and immobilized cases was very small for $h_{ac} < 0.3$. When $h_{ac} > 0.3$, however, the MNPs operate in region (II). In this case, the Néel relaxation becomes dominant and alignment of the easy axes occurs. As a result, M_3 for the suspended case became greater than that for the immobilized case for $h_{ac} > 0.3$.

Fig. 2(d) shows the M_3–h_{ac} curve for $\sigma = 20$ and $f = 3$ kHz. In this case, we obtained $h_{ac,th} = 0.23$ and $h_{ac,BR} = 0.30$. For $h_{ac} < h_{ac,BR} = 0.3$, M_3 for the suspended case became much greater than that for the immobilized case. This occurs because $1/(2\pi f) \approx \tau_{B,0}$ for $f = 3$ kHz, and the Brownian relaxation affects M_3 strongly in the suspended case. The green line shows an analytical $M_{3,BR}$–h_{ac} curve for the Brownian-dominant case [Eqs. (10) and (11)], and matched the simulation result well.

When $h_{ac} > 0.3$, the simulated value of M_3 existed between the corresponding values of $M_{3,BR}$ and $M_{3,NA}$.

Next, we study the frequency dependence of M_3 for the suspended MNPs. Fig. 3 shows the M_3–f curves obtained when f is varied from 3 to 20 kHz ($0.89 < 2\pi f \tau_{B,0} < 6$). Fig. 3(a) was obtained for $\sigma = 7$ (i.e., the Néel-dominant case). In this case, M_3 increased gradually with increasing f for all h_{ac}. The solid lines represent the analytical $M_{3,NA}$–f curves for the aligned case [Eqs. (16)–(19)], and agreed well with the simulation results.

Fig. 3(b) shows the results obtained for $\sigma = 20$. In this case, the frequency dependence of M_3 varied with h_{ac}. For $h_{ac} = 0.2$, M_3 decreased significantly with increasing f. Note that MNPs operate in region (IV) (the Brownian dominant region) for $h_{ac} = 0.2$, as shown in Fig. 1. The broken line shows the analytical $M_{3,BR}$–f curve for the Brownian-dominant case [Eqs. (10) and (11)], which matched the simulation result well for $h_{ac} = 0.2$. For high values of $h_{ac} > 0.3$, however, M_3 became weakly dependent on f. This is because the MNPs operate in region (II) (the Néel-dominant region) for $h_{ac} > 0.3$, and the frequency dependence is given by the $M_{3,NA}$–f curve. For $h_{ac} = 0.3$, the frequency dependence of M_3 was given by the dependences of $M_{3,BR}$ and $M_{3,NA}$ for $f < 5$ kHz and $f > 5$ kHz, respectively. We will discuss the frequency dependence of M_3 in more detail in Sec. 4.

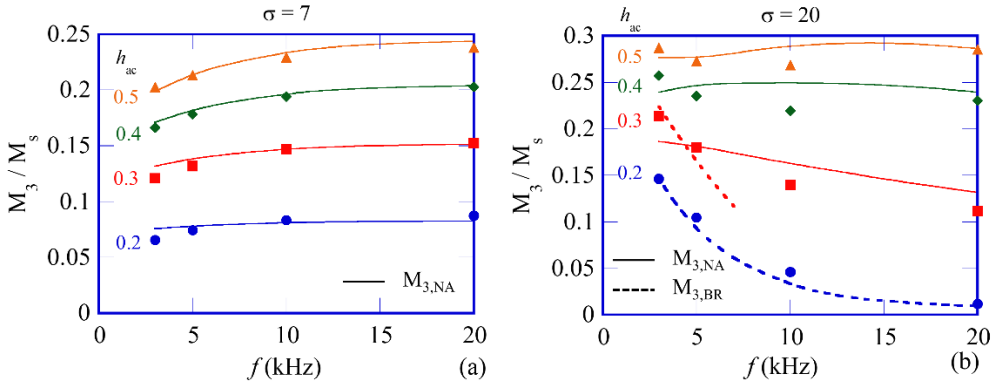

Fig. 3. Frequency dependence of M_3 for the suspended MNPs. (a) $\sigma = 7$ and (b) $\sigma = 20$. The symbols represent simulation results. The solid and broken lines represent $M_{3,NA}$ and $M_{3,BR}$, respectively.

Finally, we study the dependence of M_3 on σ, corresponding to the case where d_c varies. As shown in Fig. 1, the operating point of the MNPs moves from region (I) to regions (II)–(IV) when σ is increased. Fig. 4(a) presents the M_3–σ relationship for different values of h_{ac} when $f = 20$ kHz. Note that the MNPs operate in region (I) for $\sigma < \sigma_{th} = 10.3$. In this region, M_3 increased with increasing σ (or d_c) for all values of h_{ac}. When σ becomes greater than σ_{th}, M_3 then decreases significantly with increasing σ for $h_{ac} < 0.3$. However, when $h_{ac} > 0.3$, M_3 is weakly dependent on σ. The solid lines represent the analytical $M_{3,NA}$–σ curves for the Néel-dominant and aligned-easy-axes case [Eqs. (16)–

(19)], and agreed well with the simulation results. This agreement indicates that the effect of the Brownian relaxation is small at $f = 20$ kHz.

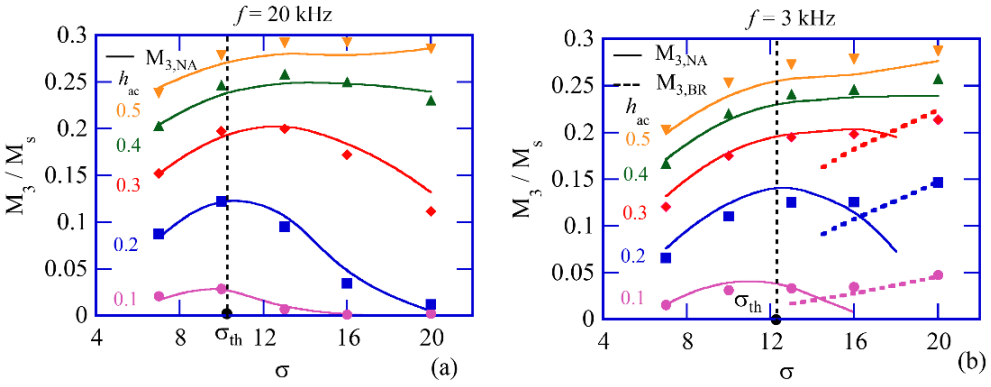

Fig. 4. Dependence of M_3 on σ. (a) f=20 kHz and (b) f = 3 kHz. Results are shown for different values of h_{ac}. The symbols represent simulation results. The solid and broken lines represent $M_{3,NA}$ and $M_{3,BR}$, respectively.

Fig. 4(b) presents the M_3–σ relationship for f = 3 kHz, where σ_{th} = 12.2. In this case, M_3 increased with increasing σ, even when $\sigma > \sigma_{th}$ and $h_{ac} < 0.3$, which is in contrast to the case when f = 20 kHz. This is because the Brownian relaxation causes M_3 to increase greatly for the suspended case when $1/(2\pi f) \approx \tau_{B,0}$. The broken lines represent the analytical $M_{3,BR}$–σ curves [Eqs. (10) and (11)], and these lines explained well the large M_3 values for the case where $\sigma > \sigma_{th}$ and $h_{ac} < 0.3$. We will discuss the M_3–σ relationship in more detail in Sec. 4.

We note that the properties of M_3 differ considerably between the Néel- and Brownian-dominant regions, as shown in Figs. 2–4. These differences must therefore be taken into account when harmonic signals are used in biosensing applications.

3.3 Higher harmonics

We studied the correlations among the harmonic signals for the suspended MNPs. We considered the case of the relatively large h_{ac}, where rich harmonic signals can be obtained. Fig. 5(a) presents the correlation between M_5 and M_3 for different values of σ, h_{ac}, and f. The closed symbols represent the results obtained when the MNPs are operated in the Néel-dominant region, i.e., when the condition $\tau_N(H) < 1/(2\pi f) << \tau_B(H)$ is satisfied. As shown in the figure, all the simulation results fall on a single curve. The open symbols represent the results obtained when the MNPs are operated in the Brownian-dominant region, i.e., when the conditions $h_{ac} < h_{ac,BR}$ and $1/(2\pi f) \approx \tau_B(H)$ are satisfied. Once more, all the simulation results fall on a different single curve. These correlations can be expressed as:

$$\frac{M_5}{M_s} = a_5 \frac{M_3}{M_s} + b_5 \left(\frac{M_3}{M_s}\right)^2 \quad (7)$$

The coefficient values are given by $a_5 = 0.12$ and $b_5 = 1.35$ for the Néel-dominant case, while $a_5 = 0.01$ and $b_5 = 1.30$ hold for the Brownian-dominant case. The solid lines in Fig. 5(a) were calculated using Eq. (7) for these two cases. Note that an M_5–M_3 curve exists between these two limiting cases for general values of σ, h_{ac}, and f.

We also obtained a similar correlation between M_5 and M_7. This correlation can be expressed as:

$$\frac{M_7}{M_s} = a_7 \frac{M_5}{M_s} + b_7 \left(\frac{M_5}{M_s}\right)^2 \quad (8)$$

where $a_7 = 0.31$ and $b_7 = 2.2$ for the Néel case, and $a_7 = 0.1$ and $b_7 = 3.1$ for the Brownian case.

Fig. 5(b) presents the correlation of phases among the harmonic signals, including the θ_5–θ_3 and θ_7–θ_3 relations. The closed and open symbols represent the results obtained for the Néel- and Brownian-dominant cases, respectively. As shown in the figure, linear relationships were obtained in all cases, and the relationship can be expressed as:

$$\theta_5 = 1.7\theta_3, \theta_7 = 2.5\theta_3 \quad (9)$$

The coefficients in Eq. (9) can be understood as follows. When the delay time of M with respect to H is T_d, the phase lag of the nth harmonic of M is then given approximately by $\theta_n = 2\pi n f T_d$. Therefore, we can expect $\theta_5/\theta_3 = 5/3 = 1.67$ and $\theta_7/\theta_3 = 7/3 = 2.33$. These values are consistent with the coefficients used in Eq. (9).

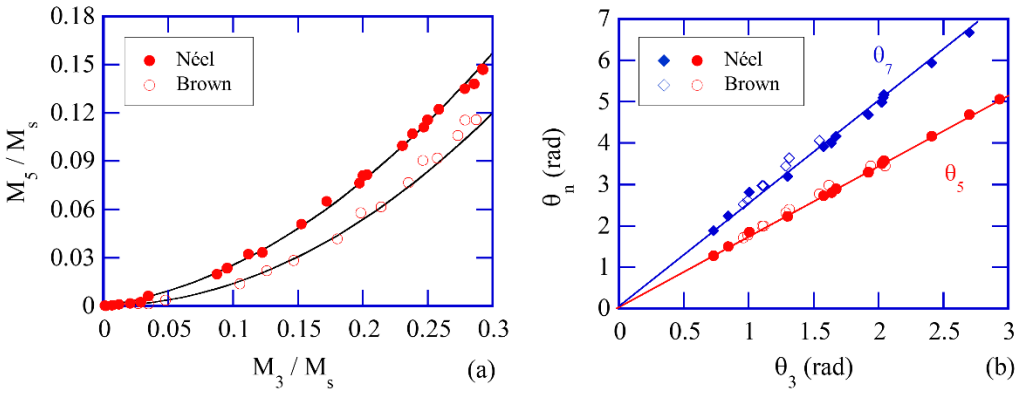

Fig. 5. Correlations among the harmonic signals for the suspended MNPs. (a) M_5–M_3 relation, and (b) θ_5–θ_3 and θ_7–θ_3 relations. Here, M_n is the amplitude, and, θ_n is the phase lag of the nth harmonics, respectively. The symbols represent simulation results, while the lines were calculated using Eqs. (7) and (9).

4. Analysis of the third harmonic signal

Now we obtain an analytical expression for the third harmonic signal of the suspended MNPs. We consider the two limiting cases here, i.e., the Brownian- and Néel-dominant cases.

4.1 MNPs dominated by Brownian relaxation

An expression for M_3 in the Brownian-dominant case, which we denote by $M_{3,\mathrm{BR}}$, was given in [16]:

$$\frac{M_{3,BR}}{M_s} = \frac{\xi_{ac}^3}{180 + 16\xi_{ac} + 12\xi_{ac}^2 + 2.36\xi_{ac}^3} \times \frac{1}{1 + \left[2\pi f \tau_{B,0} k_{m3}\right]^2} \quad (10)$$

with

$$k_{m3} = 2.15 - \frac{0.145\xi_{ac}^2}{1 + 0.187\xi_{ac} + 0.0683\xi_{ac}^2} \quad (11)$$

4.2 Immobilized MNPs with randomly oriented easy axes

Based on the simulation results, we obtained an empirical expression for M_3 for the immobilized MNPs with randomly oriented easy axes, as show below. We performed numerical simulations for $7 < \sigma < 20$, $0.1 < h_{\mathrm{ac}} < 0.5$ and 1 kHz $< f <$ 50 kHz, and clarified the dependences of the third harmonic signal on MNP parameters and excitation conditions. The symbols in Fig. 6(a) show the simulation results for the case $h_{\mathrm{ac}} > h_{\mathrm{ac,th}}$. Vertical axis represents the amplitude of the third harmonic signal, which is denoted as $M_{3,\mathrm{NR}}$, while the horizontal axis represents the parameter ξ_{e} given by

$$\xi_e = \frac{\xi_{ac}}{3.6 \times 10^{-5}\alpha^2 - 3.2 \times 10^{-3}\alpha + 1.05} \quad (12)$$

where $\alpha = \sigma \ln(f)$. Note that ξ_{e} is determined using ξ_{ac} and α.

In Fig. 6(a), different symbols correspond to different values of f. For each f value, σ and h_{ac} were varied to change ξ_{e}. As shown in the figure, all the simulation results fall on a single curve if we use the parameter ξ_{e}. We approximated the $M_{3,\mathrm{NR}}$–ξ_{e} curve as follows:

$$\frac{M_{3,NR}}{M_s} = \frac{\xi_e^3}{120 + 2\xi_e + 11\xi_e^2 + 4.32\xi_e^3} \times g_M \quad (13)$$

The function g_{M} in Eq. (13) is given by:

$$g_M = \frac{1}{1 + \exp[-2\sigma(h_{ac} - h_1)]} \quad (14)$$

with

$$h_1 = 0.12\left(h_{\mathrm{ac,th}}\right)^2 + 0.72h_{\mathrm{ac,th}} + 0.06, \quad (15)$$

where $h_{\mathrm{ac,th}}$ is given in Eq. (4)

Fig. 6(a) shows the $M_{3,\mathrm{NR}}$–ξ_{e} curve when $h_{\mathrm{ac}} > h_{\mathrm{ac,th}}$. Note that $g_{\mathrm{M}} = 1$ for $h_{\mathrm{ac}} >> h_{\mathrm{ac,th}}$. The solid

line in Fig. 6(a) was calculated using Eq. (13) with $g_M = 1$ and agrees well with the simulation results.

Fig. 6(b) shows the $M_{3,NR}$–ξ_{ac} curve obtained for $f = 20$ kHz. The symbols represent the simulation results for different values of σ. For each σ, ξ_{ac} was changed by varying h_{ac}. As shown in the figure, $M_{3,NR}$ increased gradually with increasing ξ_{ac} for $\sigma = 7$ and 10. However, for larger values of σ, $M_{3,NR}$ increased sharply when ξ_{ac} exceeded a certain value. The solid lines in Fig. 6(b) were calculated using Eq. (13). As the figure shows, we obtained good agreement between the simulation results and Eq. (13). Note that the sharp increase in $M_{3,NR}$ is given by the function g_M in Eq. (14).

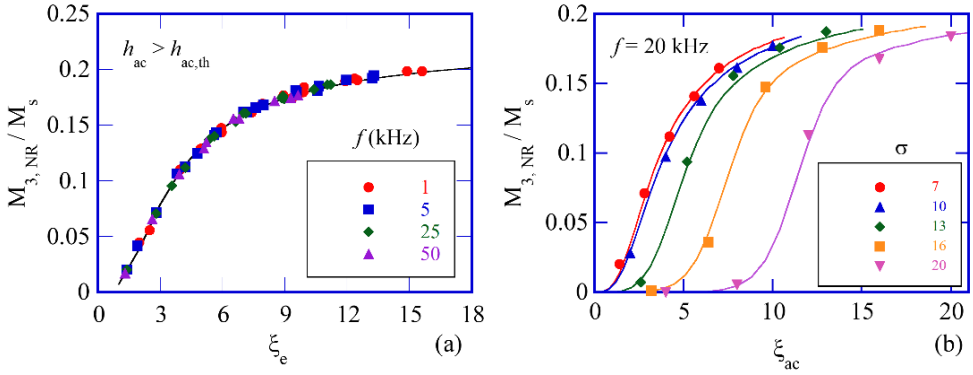

Fig. 6. $M_{3,NR}$ characteristics for the immobilized MNPs. (a) $M_{3,NR}$–ξ_e curve for the case where $h_{ac} > h_{ac,th}$. The symbols show the simulation results obtained for the different values of f, σ, and h_{ac}. The solid line was calculated using Eq. (13) with $g_M = 1$. (b) $M_{3,NR}$–ξ_{ac} curve obtained for $f = 20$ kHz and for different values of σ. The symbols represent the simulation results, while the solid lines were calculated using Eq. (13).

4.3. Immobilized MNPs with partially aligned easy axes

In regions (I) and (II) in Fig. 1, the MNPs dynamics are determined by Néel relaxation, and partial alignment of the easy axes is caused in the suspended MNPs. In this case, we showed that the AC *M*-*H* curve of the suspended MNPs can be approximated well by that for the immobilized MNPs with partially aligned easy axes [23, 27]. In the same way as used in Ref. (27), we express M_3 for this case, denoted by $M_{3,NA}$, as

$$M_{3,NA} = R_{M3} M_{3,NR} \quad (16)$$

where $M_{3,NR}$ is the third harmonic signal for the immobilized MNPs given in Eq. (13), and R_{M3} represents the increase caused by the alignment of the easy axes. We clarified the dependences of R_{M3} on MNP parameters and excitation conditions using numerical simulation for $7 < \sigma < 20$, $0.1 < h_{ac} < 0.5$, and 1 kHz $< f <$ 50 kHz. Based on the simulation results, we obtained an empirical expression as

$$R_{M3} = 1 + 1.2\tanh\left[\frac{c_3}{\sqrt{2}} k_{\text{eff}} \xi_{ac}\right] \quad (17)$$

with

$$k_{\text{eff}} = \begin{cases} \dfrac{h_{ac}}{1.15\left(1-\sqrt{\kappa}\right)}\left[0.28 + 0.009(\sigma\kappa)^2\right] & \text{for } h_{ac} < 1.15\left(1-\sqrt{\kappa}\right) \\ 0.28 + 0.009(\sigma\kappa)^2 & \text{for } h_{ac} \geq 1.15\left(1-\sqrt{\kappa}\right), \end{cases} \quad (18)$$

$$c_3 = 0.1\frac{0.55 + \exp\left(\dfrac{-6.25\sigma}{\sigma_{\text{th}}} + 7.8\right)}{1 + \exp\left(\dfrac{-6.25\sigma}{\sigma_{\text{th}}} + 7.8\right)} \times \left[1 - \exp\left(-2\pi f \tau_{B,0}/1.7\right)\right] \quad (19)$$

where $\kappa = (-1/\sigma)\ln(4\xi_{ac} f\tau_0)$ is a parameter that characterizes the Néel-dominant behavior [28, 32]. In Eq. (18), we note that $k_{\text{eff}} = 1$ for $\kappa > 1$.

Note that c_3 affects R_{M3} as shown in Eq. (17). The term $1 - \exp(-2\pi f\tau_{B,0}/1.7)$ in Eq. (19) gives the frequency dependence of c_3. We also note that c_3 is slightly dependent on $\sigma/\sigma_{\text{th}}$. When $\sigma << \sigma_{\text{th}}$ and $\sigma >> \sigma_{\text{th}}$, c_3 can be simplified to be $c_3 = 0.1[1 - \exp(-2\pi f\tau_{B,0}/1.7)]$ and $c_3 = 0.055[1 - \exp(-2\pi f\tau_{B,0}/1.7)]$, respectively.

As shown above, M_3 for the suspended MNPs can be calculated using $M_{3,\text{BR}}$ in Eq. (10) and $M_{3,\text{NA}}$ in Eq. (16) for the Brownian- and Néel-dominant cases, respectively. Next, we compare the analytical results with those from the numerical simulations. First, we compare the M_3–h_{ac} curves for the suspended MNPs. Figs. 2(a) and 2(b) show the results obtained for the Néel-dominant case ($\sigma = 7$). In this case, the simulation results for M_3 agreed with $M_{3,\text{NA}}$ in Eq. (16) for all h_{ac} values. Note, however, that $M_{3,\text{NA}}$ for $f = 3$ kHz became smaller than that for $f = 20$ kHz. This difference can be explained using the term $1 - \exp(-2\pi f\tau_{B,0}/1.7)$ in c_3 [Eq. (19)]. This term becomes 1 for $f = 20$ kHz because $2\pi f\tau_{B,0} >> 1$. However, the term becomes smaller than 1 for $f = 3$ kHz because $2\pi f\tau_{B,0} = 0.89$ in that case. As a result, c_3 becomes small for $f = 3$ kHz. This small c_3 results in a small $M_{3,\text{NA}}$, as can be seen from Eq. (17).

Figs. 2(c) and 2(d) show the results for $\sigma = 20$. In this case, M_3 agreed with $M_{3,\text{NA}}$ or $M_{3,\text{BR}}$, depending on the values of h_{ac} and f. M_3 for $f = 20$ kHz agreed well with $M_{3,\text{NA}}$ for all h_{ac}. When $f = 3$ kHz, M_3 agreed well with $M_{3,\text{BR}}$ for $h_{\text{ac}} < h_{\text{ac,BR}}$, while M_3 was between $M_{3,\text{BR}}$ and $M_{3,\text{NA}}$ when $h_{\text{ac}} > h_{\text{ac,BR}}$.

Fig. 3 shows the M_3–f relationship. As shown in Fig. 3(a), the results for $\sigma = 7$ agreed well with the $M_{3,\text{NA}}$–f relationship calculated using Eqs. (16)–(19). Note that the frequency dependence of $M_{3,\text{NA}}$ is mainly given by the term $1 - \exp(-2\pi f\tau_{B,0}/1.7)$ in c_3 [Eq. (19)]. For $\sigma = 20$, the frequency dependence varied considerably with h_{ac}, as shown in Fig. 3(b). For $h_{\text{ac}} = 0.2$, M_3 decreased significantly with increasing f, with a dependence that agreed with the $M_{3,\text{BR}}$–f relationship calculated using Eq. (10). Note that the frequency dependence of $M_{3,\text{BR}}$ is mainly given by the term $[1 + (2\pi f\tau_{B,0}k_{\text{m3}})^2]^{-1}$ in Eq. (10). For $h_{\text{ac}} > 0.3$, however, the frequency dependence of M_3 can be better

explained using the $M_{3,NA}$–f curve.

Fig. 4 presents the M_3–σ relationship. As shown in Fig. 4(a), the simulation results for f = 20 kHz can be explained well by the $M_{3,NA}$–σ curves for all values of σ and h_{ac} because the effect of the Brownian relaxation can be neglected in this case. For f = 3 kHz, however, M_3 becomes large even for the cases where h_{ac} is low ($h_{ac} < 0.3$) and σ is high ($\sigma > \sigma_{th}$), as shown in Fig. 4(b). This is because the Brownian relaxation contributes greatly to M_3 when f = 3 kHz. In these cases, the M_3–σ relations approached those of the $M_{3,BR}$–σ curves (represented by the broken lines).

4.4 Phase

When the MNPs are operated in the Brownian-dominant region, i.e., in region (IV), the following expression for θ_3, which is denoted by $\theta_{3,BR}$, was obtained in [16]:

$$\theta_{3,BR} = 3\tan^{-1}\left(2\pi k_{\theta 3} f \tau_{B,0}\right) \quad (20)$$

with

$$k_{\theta 3} = 1.31 - \frac{0.0496\xi_{ac}^2}{1 + 0.222\xi_{ac} + 0.0435\xi_{ac}^2} \quad (21)$$

When the MNPs are operated in the Néel-dominant region, i.e., in regions (I) and (II), it has been demonstrated that the parameter $\kappa = (-1/\sigma)\ln(4\xi_{ac} f \tau_0)$ affects the delay time of M with respect to H [28, 32]. Therefore, we studied the relationship between θ_3 and κ in this case. In the simulation, κ is changed by varying σ, h_{ac}, and f. Based on the simulation results, we obtained an empirical expression for θ_3 for the immobilized MNPs, denoted by $\theta_{3,NR}$, as follows.

$$\theta_{3,NR} = \begin{cases} 1.7(1-\kappa^{0.6})h_{ac}^{-1.25} \times g_P & \text{for } \kappa < 0.6 \\ 1.2\exp\left[-\left(\dfrac{\kappa}{0.6}\right)^{2.3}\right] h_{ac}^{-1.25} \times g_P & \text{for } \kappa > 0.6 \end{cases} \quad (22)$$

with

$$g_P = \frac{1}{1 + \exp[-25(h_{ac} - h_1/2)]} \quad (23)$$

Note that $g_P = 1$ for $h_{ac} >> h_{ac,th}$. Fig. 7(a) shows the θ_3–κ relation when $h_{ac} >> h_{ac,th}$. Open circles represent the results obtained for the immobilized MNPs for different values of σ, h_{ac}, and f. The vertical axis is expressed in terms of $\theta_3 h_{ac}^{1.25}$. As shown, the simulation results all fall on a single curve. The two lines were calculated using Eq. (22) with $g_P = 1$ for $\kappa < 0.6$ and $\kappa > 0.6$. As shown in the figure, the simulation results can be calculated using Eq. (22).

Fig. 7(b) shows the θ_3–h_{ac} curves for the immobilized MNPs. The symbols represent the simulation results obtained for different values of σ and f = 20 kHz. As shown, θ_3 decreased gradually with increasing h_{ac} for σ = 10 and 13. However, for σ = 16 and 20, θ_3 showed peaks at specific values of h_{ac}. The solid lines in Fig. 7(b) were calculated using Eqs. (22) and (23) and match the θ_3–h_{ac} curves well.

The closed symbols shown in Fig 7(a) were the results obtained for the suspended MNPs. As shown, the $\theta_3 h_{ac}^{1.25}$–κ relations are almost on the same curve between the immobilized and suspended MNPs. This result indicates that θ_3 for the suspended MNPs, i.e., $\theta_{3,NA}$, can be approximated with that of the immobilized MNPs, i.e., $\theta_{3,NA} \approx \theta_{3,NR}$. Note, however, that the error of this approximation increases with decreasing κ.

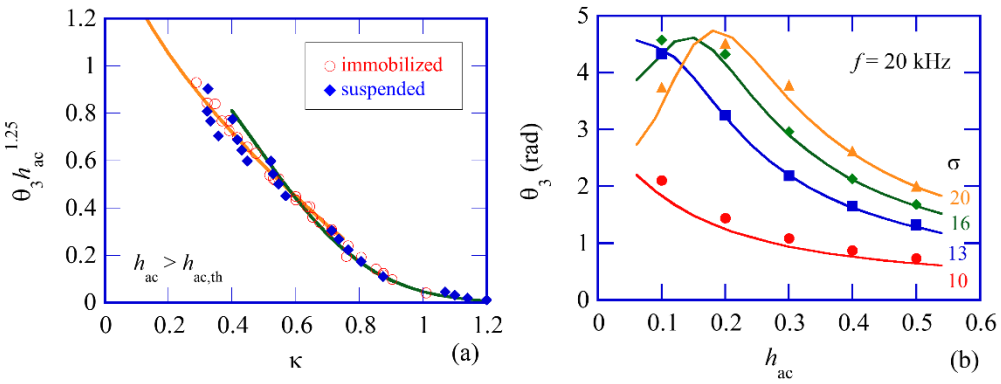

Fig. 7. (a) Relationship between θ_3 and κ for $h_{ac} > h_{ac,th}$. The open and closed symbols represent the simulation results for the immobilized and suspended MNPs, respectively. The two lines were calculated using Eq. (22) with $g_P = 1$. (b) θ_3–h_{ac} curves for the immobilized MNPs. The symbols show the results for different σ and f = 20 kHz, and the lines were calculated using Eqs. (22) and (23).

5. Experimental

We now compare the theoretical results with the experimental results obtained using the Synomag sample. The magnetic parameters of the sample were estimated to be M_s = 345 kA/m and K =9.7 kJ/m^3 [15]. Note that d_c is distributed within the sample. Fig. 8(a) presents the d_c distribution that was estimated from the DC M-H curve using the procedure presented in our previous paper [15]. In Fig. 8(a), the horizontal axis is expressed in terms of σ rather than d_c; the value of K = 9.7 kJ/m^3 was then used to obtain σ from d_c. The left-hand side of the vertical axis represents the value of $n(d_c)V_c$, where $n(d_c)$ is the number density of the MNPs with d_c per unit of MNPs volume. As shown in Fig. 8(a), σ was mainly distributed from 2 to 25, and $n(d_c)V_c$ had a peak value at σ = 7; in other words, d_c was distributed from 12 to 28 nm, and $n(d_c)V_c$ had a peak value at d_c = 18 nm. The right-hand side of the vertical axis represents the fraction V_F given by

$$V_F = \int_0^{d_c} n(d_c')\, V_c dd_c' \quad (24)$$

We consider the case where the sample is excited at f = 20 kHz. In this case, we obtain σ_{th} = 10.3 from Eq. (3). As shown in Fig. 1, MNPs with $\sigma < \sigma_{th}$ operated in region (I) (a Néel-dominant region),

while MNPs with $\sigma > \sigma_{th}$ operated in regions (II)–(IV) (Néel- or Brownian-dominant regions). As shown in Fig. 8(a), we obtained $V_F = 0.76$ at $\sigma = \sigma_{th} = 10.3$. Therefore, the volume fraction of MNPs in region (I) is 0.76, while the fraction of the MNPs in regions (II)–(IV) is 0.24. This means that the magnetic properties of the Synomag sample are primarily affected by Néel relaxation.

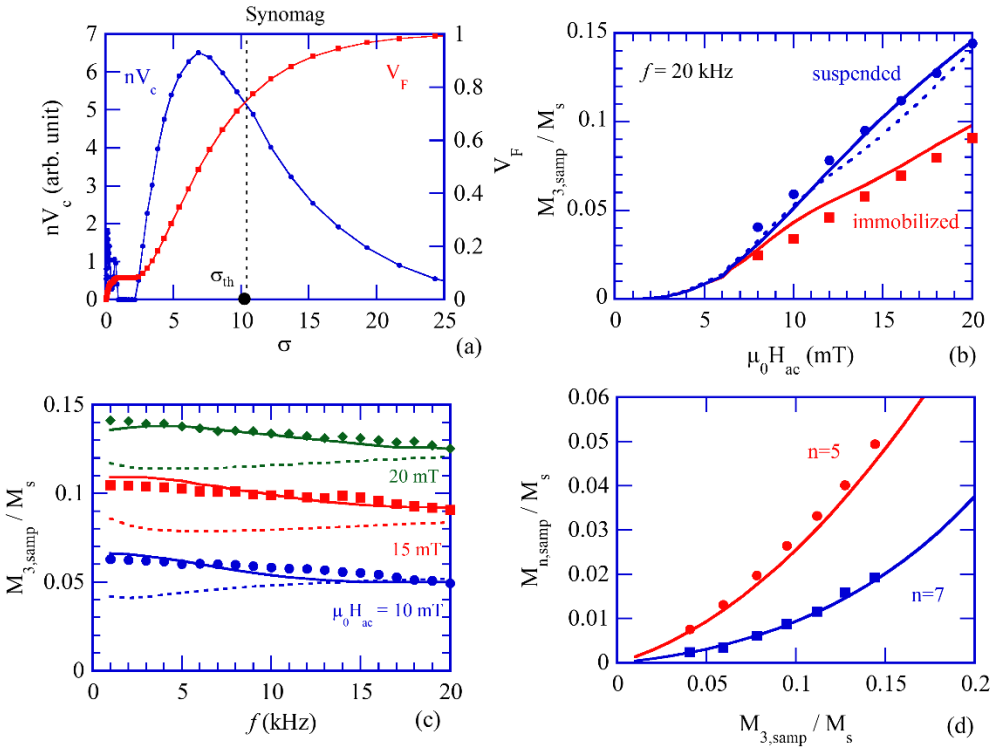

Fig. 8. Comparison between results of the experiments and the analysis for the Synomag sample. (a) Distribution of the magnetic core size d_c. (b) $M_{3,samp}$–H_{ac} relationship for $f = 20$ kHz. (c) Frequency dependence of $M_{3,samp}$. (d) Relationship between $M_{3,samp}$ and $M_{n,samp}$ (where $n = 5$ and 7). The symbols in (b)-(d) represent the experimental results, while the lines represent the analytical results.

In this study, we use a two-particle approximation for simplicity, and make a semi-quantitative comparison between experiment and the analysis. In Fig. 8(a), MNPs with $\sigma < \sigma_{th}$ are represented by an MNP with $\sigma = 7$; $n(d_c)V_c$ showed a peak value at $\sigma = 7$. MNPs with $\sigma > \sigma_{th}$ are represented by an MNP with $\sigma = 15$. In this approximation, the third harmonic signal of the sample is given by:

$$\overrightarrow{M_{3,samp}} = a\overrightarrow{M_3(7)} + b\overrightarrow{M_3(15)} \quad (25)$$

where $\overrightarrow{M_{3,samp}} = \left(M_{3,samp}\cos\theta_{3,samp}, M_{3,samp}\sin\theta_{3,samp}\right)$ is a vector that represents the real and imaginary parts of the third harmonic signal of the sample, and $\overrightarrow{M_3}(7)$ and $\overrightarrow{M_3}(15)$ are the harmonic signals for the MNP with $\sigma = 7$ and 15, respectively. The parameters a and b represent the volume fractions of the two particles. Note that the real and imaginary parts of $\overrightarrow{M_{3,samp}}$ can be obtained using

Eq. (25) and the amplitude $M_{3,\mathrm{samp}}$ can then be calculated.

First, we measured the AC $M-H$ curve for various H_{ac} when f = 20 kHz. The circles and rectangles in Fig. 8(b) represent the $M_{3,\mathrm{samp}}-H_{\mathrm{ac}}$ relations for the suspended and immobilized samples, respectively. As shown in the figure, the difference in $M_{3,\mathrm{samp}}$ between the two samples increases with increasing H_{ac}, and this result resembles the simulation result presented in Fig. 2(a).

The lines in Fig. 8(b) were calculated using Eq. (25). The red line represents the result for the immobilized sample. In the calculations, the real and imaginary parts of $\overrightarrow{M_3}(7)$ and $\overrightarrow{M_3}(15)$ were calculated using the amplitude $M_{3,\mathrm{NR}}$ in Eq. (13) and the phase $\theta_{3,\mathrm{NR}}$ in Eq. (22). The values of a and b were taken as adjustable parameters. As shown in Fig. 8(b), we obtained reasonable agreement between the experiments and the analysis for a = 0.8 and b = 0.1. The value of a = 0.8 is consistent with the volume fraction of 0.76 for the MNPs in region (I). However, the value of b = 0.1 is smaller than the volume fraction of 0.24 for the MNPs in regions (II)–(IV).

The blue lines in Fig. 8(b) represent the results for the suspended sample. In this case, $\overrightarrow{M_3}(7)$ was calculated using $M_{3,\mathrm{NA}}$ in Eq. (16) and $\theta_{3,\mathrm{NR}}$ in Eq. (22); note that we approximated $\theta_{3,NA} \approx \theta_{3,NR}$, as shown in Fig. 7(a). For $\overrightarrow{M_3}(15)$, we considered two cases. The first was the case where an MNP with σ = 15 is operating in the Néel-dominant region, and $\overrightarrow{M_3}(15)$ is calculated using $M_{3,\mathrm{NA}}$ in Eq. (16) and $\theta_{3,\mathrm{NR}}$ in Eq. (22). The broken line in Fig. 8(b) represents the result calculated for this case with a = 0.8 and b = 0.1. As shown, we obtained reasonable agreement between the experiments and the analysis.

The second is the case where an MNP with σ = 15 is operating in the Brownian-dominant region, and $\overrightarrow{M_3}(15)$ is calculated using $M_{3,\mathrm{BR}}$ in Eq. (10) and $\theta_{3,\mathrm{BR}}$ in Eq. (20). The solid line represents the calculated result for this case. In the calculation, the value of d_{H} was taken as an adjustable parameter. As shown in Fig. 8(b), we obtained good agreement between the experiments and the analysis when we took d_{H} = 30 nm.

Next, Fig. 8(c) shows the frequency dependence of $M_{3,\mathrm{samp}}$ when f was varied from 1 to 20 kHz. The results for $\mu_0 H_{\mathrm{ac}}$ = 10, 15 and 20 mT are shown. The broken lines were obtained when $\overrightarrow{M_3}(15)$ was calculated using $M_{3,\mathrm{NA}}$ and $\theta_{3,\mathrm{NR}}$ (the Néel-dominant case). In this case, the analytical value of $M_{3,\mathrm{samp}}$ was almost independent of f. The solid lines were obtained when $\overrightarrow{M_3}(15)$ was calculated using $M_{3,\mathrm{BR}}$ and $\theta_{3,\mathrm{BR}}$ (the Brownian-dominant case). In this case, the analytical value of $M_{3,\mathrm{samp}}$ decreased with increasing f, and agreed well with the experimental characteristic. This result suggests that the representative MNP with σ = 15 operates in the Brownian-dominant region.

We note that the value of d_{H} = 30 nm obtained in Figs. 8(b) and 8(c) was smaller than the nominal value of d_{H} = 50 nm given by the supplier. We measured the d_{H} distribution for the Synomag sample using dynamic light scattering (DLS) measurement. Intensity distribution measured with DLS had a peak value at d_{H}=51 nm, which is in good agreement with the nominal value of d_{H}=50 nm. We note that the intensity distribution gives the $n(d_{\mathrm{H}})(V_{\mathrm{H}})^2$ vs d_{H} curve, where $n(d_{\mathrm{H}})$ is the number density of

the MNPs with d_H. On the other hand, the volume distribution, i.e., the $n(d_H)V_H$ vs d_H curve, had a peak value at d_H=37 nm. The number distribution, i.e., the $n(d_H)$ vs d_H curve, had a peak value at d_H=33 nm, which is close to the value d_H=30 nm obtained in Figs. 8(b) and 8(c). This is reasonable because the d_H value affects only the frequency dependence of $M_{3,BR}$ through $\tau_{B,0}$ as shown in Eq. (10), and the Brownian relaxation of MNPs is affected by the $n(d_H)$ vs d_H curve when d_H distributes, as discussed in ref. (33).

Finally, Fig. 8(d) shows the correlation between $M_{3,samp}$ and $M_{n,samp}$ (where n = 5 and 7). The symbols represent the experimental results, while the lines represent the analytical results calculated using Eqs. (7) and (8). In the calculations, we used the coefficients a_5, b_5, a_7, and b_7 for the Néel-dominant case because the magnetic properties of the Synomag sample are primarily affected by the Néel relaxation, as indicated in Fig. 8(a). As shown, we obtained good agreement between the experiments and the analysis.

As shown above, the experimental results can be explained semi-quantitatively using a two-particle approximation. For a more quantitative analysis, however, we will have to take the distributions of both d_c and d_H into account. For the MNPs sample dominated by Néel relaxation, accurate estimation of the d_c distribution is sufficient. For the MNPs samples dominated by Brownian relaxation, accurate estimation of the d_H distribution is also necessary, as discussed in Refs. (33) and (34). It will be our future work to make quantitative comparison for samples with different degree of Brownian and Néel relaxation.

6. Conclusions

We studied the harmonic signals of MNPs suspended in solution. First, we presented the condition that determines whether Brownian or Néel relaxation becomes dominant. We emphasized that the MNP's behavior changes from Brownian-dominant to Néel-dominant when the field amplitude H is varied, even for fixed MNP parameters. The different properties of the third harmonic signal for the Brownian- and Néel-dominant cases were clarified. The relationships among the higher harmonic signals were also presented. Next, analytical expressions for the third harmonic signal were obtained for both the Brownian- and Néel-dominant cases. In the Néel-dominant case, the alignment of the easy axes caused by the AC field was taken into account. The obtained expressions explain well the dependence of the third harmonic signal on the MNP parameters and the excitation conditions. Finally, the analytical results were compared semi-quantitatively with experimental results, and reasonable agreement was obtained between them. The results obtained in this work will be useful for biosensing applications of MNPs.

CRediT authorship contribution statement

Keiji Enpuku: Writing - Original draft. **Yi Sun**: Investigation. **Haochen Zhang**: Investigation. **Takashi Yoshida**: Supervision.

Declaration of competing interest

The authors declare that they have no known competing financial interests or personal relationships that could have appeared to influence the work reported in this paper.

Data availability

Data will be made available on request.

Acknowledgements

This work was supported in part by the Japan Society for the Promotion of Science (JSPS) KAKENHI [grant numbers JP20H05652, JP21H01343].

References

1. L. R. Croft, P. W. Goodwill, J. J. Konkle, H. Arami, D. A. Price, A. X. Li, E. U. Saritas, S. M. Conolly, "Low drive field amplitude for improved image resolution in magnetic particle imaging", *Medical physics*, **43**, 424 (2016). https://doi.org/10.1118/1.4938097
2. ZW. Tay, P. Chandrasekharan, XY. Zhou, E. Yu, B. Zheng, and S.Conolly, "In vivo tracking and quantification of inhaled aerosol using magnetic particle imaging towards inhaled therapeutic monitoring", *Theranostics* **8**, 3676-3687 (2018); doi: 10.7150/thno.26608
3. L. C. Wu, Y. Zhang, G. Steinberg, H. Qu, S. Huang, M. Cheng, T. Bliss, F. Du, J. Rao, G. Song, L. Pisani, T. Doyle, S. Conolly, K. Krishnan, G. Grant and M. Wintermark, "A review of magnetic particle imaging and perspectives on neuroimaging", *American Journal of Neuroradiology,* **40**, 206-212 (2019); DOI: https://doi.org/10.3174/ajnr.A5896
4. M. Graeser, F. Thieben, P. Szwargulski, F. Werner, N. Gdaniec, M. Boberg, F. Griese, M. Möddel, P. Ludewig, D. van de Ven, O. M. Weber, O. Woywode, B. Gleich, and T. Knopp "Human-sized magnetic particle imaging for brain applications", *Nat. Commun.* **10**, 1936 (2019). https://doi.org/10.1038/s41467-019-09704-x
5. H. Paysen, N. Loewa, A. Stach, J. Wells, O. Kosch, S. Twamley, M. R. Makowski, T. Schaeffter, A. Ludwig, F. Wiekhorst, "Cellular uptake of magnetic nanoparticles imaged and quantified by magnetic particle imaging", *Sci Rep* **10,** 1922 (2020). https://doi.org/10.1038/s41598-020-58853-3
6. K. Wu, D. Su, R. Saha, J. Liu, V. K. Chugh, and Jian-Ping Wang, "Magnetic particle spectroscopy: A short review of applications using magnetic nanoparticles", *ACS Appl. Nano Mater.* **3**, 4972–4989 (2020). https://doi.org/10.1021/acsanm.0c00890
7. J. Fock, M. Parmvi, M. Strömberg, P. Svedlindh, M. Donolato, M. F. Hansen, "Comparison of optomagnetic and AC susceptibility readouts in a magnetic nanoparticle agglutination assay for detection of C-reactive protein", *Biosensors and Bioelectronics*, **88**, 94-100 (2017). https://doi.org/10.1016/j.bios.2016.07.088
8. K. Enpuku1, M. Shibakura, Y. Arao, T. Mizoguchi, A. Kandori, M. Hara and K. Tsukada, "Wash-free detection of C-reactive protein based on third-harmonic signal measurement of magnetic markers", *Jpn. J. Appl. Phys.* **57**, 090309 (2018). https://doi.org/10.7567/JJAP.57.090309
9. J.-J. Chieh, W.-C. Wei, S.-H. Liao, H.-H. Chen, Y.-F. Lee, F.-C. Lin, M.-H. Chiang, M.-J. Chiu, H.-E. Horng, and S.-Y. Yang, "Eight-channel AC magnetosusceptometer of magnetic nanoparticles for high-throughput and ultra-high-sensitivity immunoassay", *Sensors* **18**, 1043 (2018). https://doi.org/10.3390/s18041043
10. J. Zhong, E. L. Rösch, T. Viereck, M. Schilling, and F. Ludwig, "Toward rapid and sensitive detection of SARS-CoV-2 with functionalized magnetic nanoparticles", *ACS Sens.* **6**, 976–984 (2021). https://doi.org/10.1021/acssensors.0c02160

11. J. Zhong, K-J Janssen, S. Draack, T. Viereck, M. Schilling, and F. Ludwig, “Dependence of biomolecule detection on magnetic nanoparticle concentration”, *J. Magn. Magn. Mater.* **517**, 167408 (2021); https://doi.org/10.1016/j.jmmm.2020.167408.
12. V. K. Chugh, A. di Girolamo, V. D. Krishna, K. Wu, M. C-J Cheeran, and J-P Wang, “Frequency and amplitude optimizations for magnetic particle spectroscopy applications”, *J. Phys. Chem. C* (2022); https://doi.org/10.1021/acs.jpcc.2c07534
13. X. Cui, L. Li and W. Liu, "A Rapid and Sensitive Magnetic Immunoassay of Biomolecules Based on Magnetic Nanoparticles”, *IEEE Trans. Instr. Meas.* **71**, 6007407 (2022); doi: 10.1109/TIM.2022.3216405.
14. C. Shasha,and K. M. Krishnan, “Nonequilibrium dynamics of magnetic nanoparticles with applications in biomedicine”, *Adv. Mater.* **33**, 1904131 (2021). https://doi.org/10.1002/adma.201904131
15. K. Enpuku, S. Yamamura, T. Yoshida, “Quantitative explanation of the difference in AC magnetization curves between suspended and immobilized magnetic nanoparticles for biomedical application, *J. Magn. Magn. Mater.* **564**, 170089 (2022). https://doi.org/10.1016/j.jmmm.2022.170089.
16. T. Yoshida1, K. Ogawa1, K. Enpuku, N. Usuki, and H. Kanzaki, “AC susceptibility of magnetic fluid in nonlinear Brownian relaxation region: Experiment and comparison with numerical simulation”, *Jpn. J. Appl. Phys*. **49**, 053001 (2010). https://doi.org/10.1143/JJAP.49.053001
17. H. Mamiya, and B. Jeyadevan, “Hyperthermic effects of dissipative structures of magnetic nanoparticles in large alternating magnetic fields”, *Sci Rep* **1**, 157 (2011). DOI: 10.1038/srep00157
18. S. B. Trisnanto, S. Ota and Y. Takemura,” Two-step relaxation process of colloidal magnetic nanoclusters under pulsed fields”, *Appl. Phys. Express* **11** 075001 (2018). DOI: 10.7567/APEX.11.075001
19. M. Suwa, A. Uotani, and S. Tsukahara, “Magnetic and viscous modes for physical rotation of magnetic nanoparticles in liquid under oscillating magnetic field”, *Appl. Phys. Lett.* **116**, 262403 (2020); https://doi.org/10.1063/5.0010095
20. S. A. Shah, D. B. Reeves, R. M. Ferguson, J. B. Weaver, and K. M. Krishnan, "Mixed Brownian alignment and Néel rotations in superparamagnetic iron oxide nanoparticle suspensions driven by an ac field”, *Phys. Rev.* **B 92**, 094438 (2015). https://doi.org/10.1103/PhysRevB.92.094438
21. T. Yoshida, S. Bai, A. Hirokawa, K. Tanabe, K. Enpuku, “Effect of viscosity on harmonic signals from magnetic fluid”, *J. Magn. Magn. Mater.* **380**, 105-110 (2015). https://doi.org/10.1016/j.jmmm.2014.10.044
22. Ahmed L. Elrefai, K. Enpuku, and T. Yoshida, “Effect of easy axis alignment on dynamic magnetization of immobilized and suspended magnetic nanoparticles”, *J. Appl. Phys*. **129**, 093905

(2021); https://doi.org/10.1063/5.0041215

23. K. Enpuku, Ahmed L. Elrefai, J. Gotou, S. Yamamura, T. Sasayama and T. Yoshida, "Difference in AC magnetization between suspended and immobilized magnetic nanoparticles in Néel-relaxation dominant case: Effect of easy axis alignment in suspended nanoparticles", *J. Appl. Phys.* **130**, 113903 (2021); https://doi.org/10.1063/5.0056481
24. S. Draack, T. Viereck, F. Nording, K.-J. Janssen, M. Schilling, F. Ludwig, "Determination of dominating relaxation mechanisms from temperature-dependent Magnetic Particle Spectroscopy measurements", *J. Magn. Magn. Mater.* **474**, 570-573 (2019). https://doi.org/10.1016/j.jmmm.2018.11.023.
25. S. Ota, Y. Matsugi, T. Nakamura, R. Takeda, Y. Takemura, I. Kato, S. Nohara, T. Sasayama, T. Yoshida, K. Enpuku, "Effects of size and anisotropy of magnetic nanoparticles associated with dynamics of easy axis for magnetic particle imaging", *J. Magn. Magn. Mater.* **474**, 311-318 (2019). https://doi.org/10.1016/j.jmmm.2018.11.043.
26. Hannes Albers, Tobias Kluth, Tobias Knopp, "Simulating magnetization dynamics of large ensembles of single domain nanoparticles: Numerical study of Brown/Néel dynamics and parameter identification problems in magnetic particle imaging", *J. Magn. Magn. Mater.* 541, 168508 (2022); https://doi.org/10.1016/j.jmmm.2021.168508.
27. K. Enpuku, and Takashi Yoshida, "Dependence of hysteresis loss of immobilized magnetic nanoparticles on the easy-axis angle: Effect of easy-axis alignment", *AIP Advances* **12**, 055211 (2022); https://doi.org/10.1063/5.0090915
28. N. A. Usov and B. Ya. Liubimov, "Dynamics of magnetic nanoparticle in a viscous liquid: Application to magnetic nanoparticle hyperthermia, *J. Appl. Phys*. **112**, 023901 (2012); https://doi.org/10.1063/1.4737126
29. T. Sasayama1, T. Yoshida1 and K. Enpuku, "Relationship between harmonic spectra and coercive field of immobilized magnetic nanoparticles", *Jpn. J. Appl. Phys.* **56** 025001 (2017): DOI 10.7567/JJAP.56.025001
30. J. Dieckhoff, D. Eberbeck, M. Schilling, F. Ludwig, "Magnetic-field dependence of Brownian and Néel relaxation times", *J. Appl. Phys.* **119**, 043903 (2016). https://doi.org/10.1063/1.4940724
31. W.T. Coffey, P.J. Cregg, Y.U.P. Kalmykov, "On the Theory of Debye and Néel Relaxation of Single Domain Ferromagnetic Particles", in: *Adv. Chem. Phys*., Wiley-Blackwell, 2007: pp. 263–464. doi:10.1002/9780470141410.ch5.
32. J. Carrey, B. Mehdaoui, and M. Respaud, "Simple models for dynamic hysteresis loop calculations of magnetic single-domain nanoparticles: Application to magnetic hyperthermia optimization", *J. Appl. Phys.* **109**, 083921 (2011); https://doi.org/10.1063/1.3551582
33. F. Ludwig, C. Balceris, C. Jonasson and C. Johansson, "Analysis of AC susceptibility spectra for the characterization of magnetic nanoparticles," *IEEE Trans. Magn*. **53**, 6100904 (2017); doi:

10.1109/TMAG.2017.2693420.

34. T. Yoshida, K. Ogawa, A. K. Bhuiya, and K. Enpuku, “Nonlinear behavior of magnetic fluid in Brownian relaxation”, *AIP Conference Proceedings,* **1311**, 102–110 (2010); https://doi.org/10.1063/1.3529998